Redox Biology 84 (2025) 103665

Contents lists available at ScienceDirect

Redox Biology

journal homepage: www.elsevier.com/locate/redox

Targeting MYOF suppresses pancreatic ductal adenocarcinoma progression by inhibiting ILF3-LCN2 signaling through disrupting OTUB1-mediated deubiquitination of ILF3

Zhihui Li [a,1], Jianlei Zhang [a,1], Jiang Yin [a,1], Wen Ma [a], Hongfan Liao [a], Lv Ling [a], Qingfeng Zou [a], Yabing Cao [b], Ying Song [a], Guopei Zheng [a], Xiaoye Hu [a,*], Guohua Yang [a,**], Nan Li [a,***]

[a] Guangzhou Institute of Cancer Research, The Affiliated Cancer Hospital, Guangzhou Medical University; Guangdong Provincial Key Laboratory of Protein Modification and Degradation, Hengzhigang Road 78#, Guangzhou, 510095, Guangdong, China
[b] Kiang Wu Hospital, Macao Special Administrative Region of China

ARTICLE INFO

Keywords:
Pancreatic cancer
MYOF
OTUB1
ILF3
LCN2
Ferroptosis

ABSTRACT

Pancreatic ductal adenocarcinoma (PDAC) is still a highly aggressive and fatal disease. The molecular mechanisms for PDAC progression are still not fully understood. Here, we demonstrated the overexpression of MYOF in PDAC in multiple sample sets, which is significantly associated with poor outcome of PDAC patients. MYOF knockout suppresses PDAC progression in vitro and in vivo. MYOF knockout exerts its effects by promoting ferroptosis via downregulating LCN2 expression. Ectopic LCN2 expression overcame the effects of MYOF knockout in PDAC cells. Mechanistically, MYOF respectively recruits OTUB1 and ILF3 to enhance their interaction and relieves ILF3 protein ubiquitination and degradtion. MYOF maintains ILF3 protein stability, thereby enhances ILF3 interacting with and improving LCN2 mRNA stability. Moreover, we screened and identified natural compound Picroside II potentially targets MYOF to suppress PDAC progression. These findings uncover the biological roles and mechanisms of MYOF and preliminarily indicate the potential of targeting MYOF in PDAC progression, highlighting a novel therapeutic strategy for PDAC.

1. Introduction

Pancreatic cancer mostly characterized as pancreatic ductal adenocarcinoma (PDAC) accounting for greater than 90 % still remains a clinically challenging cancer type. According to the Global Cancer Observatory (GLOBOCAN) 2020, pancreatic cancer related death ranked the seventh leading cause of cancer death among all malignant tumors [1]. PDAC as a deadly disease is predicted to be the second leading cause of cancer death in the United States by 2030 [2]. In the past decade, based on basic and translational investigations remarkable progress has been made in treating PDAC including refinement of the surgical techniques and improvements in adjuvant and neoadjuvant therapies as chemotherapy and target therapy. Despite this remarkable progress, PDAC is still a highly aggressive cancer with an overall 5-year relative survival rate of about 10 % due to both its late stage at diagnosis and poor response to current therapy [2,3]. Thus, growing understanding molecular mechanisms for biology and treatment response, and exploring novel and effective therapies are urgently required.

Generally, the risk factors for PDAC development and progression can be categorized as individual characteristics such as DNA variants, lifestyle and environment, and disease status including diabetes mellitus, obesity and chronic pancreatitis [3–5]. In molecular biology, PDAC forms from the exocrine tissue of the pancreas by drivers evolving through a series of histopathologic changes referred to as dysplastic precursor lesions or pancreatic intraepithelial neoplasias (PanIN0, toward invasive and finally metastatic pancreatic cancer [6]. So far, the most commonly documented drivers were the activating mutation of *KRAS* as oncogene and function-loss mutation of *CDKN2A*, *TP53* and

* Corresponding author.
** Corresponding author.
*** Corresponding author.
E-mail addresses: hxiaoye@126.com (X. Hu), yangguohuadr@163.com (G. Yang), Linan_gz2013@163.com (N. Li).
[1] contributed equally.

https://doi.org/10.1016/j.redox.2025.103665
Received 3 April 2025; Received in revised form 28 April 2025; Accepted 5 May 2025
Available online 11 May 2025

SMAD4 as tumor suppressors using genetically engineered mouse models and detection on clinical tissue samples [6–8]. Additionally, the critical function of epigenetic modifiers such as miRNAs and LncRNAs is also emphasized in PDAC [9]. Recently, MYOF was reported to be overexpressed in PDAC and correlated with overall survival. MYOF was required to maintain branched mitochondrial structure and a high oxidative phosphorylation activity [10]. MYOF has been shown to maintain lysosomal integrity and support tumor growth in PDAC [11]. MYOF is a member of the ferlin family, large proteins (200–240 kDa) with multiple C2 structural domains that play important roles in vesicle fusion and receptor trafficking [12]. In recent years, there has been increasing evidence that MYOF is over-expressed in a variety of tumors and is associated with poor prognosis [13,14]. However, the molecular mechanism for MYOF involvement in PDAC progression and the translational implication remain to be further elucidated.

In the present study, we using a series online data including single-cell RNA sequencing data confirmed the overexpression of MYOF in PDAC cells. MYOF deletion inhibited PDAC progression and induced ferroptosis via downregulating LCN2 expression. The biological function and molecular mechanisms for MYOF in PDAC were elucidated via a series of experimental models. The potential of targeting MYOF in PDAC control was also preliminarily explored.

2. Materials and methods

2.1. Cell culture

The human pancreatic ductal epithelial cell line HPNE, four human pancreatic cancer (PC) cell lines (CFPAC-1, and BxPC-3, SW1990, PANC-1), and two mouse PC cell lines (LTPA and Panc02) were purchased from the Procell Life Science & Technology (Wuhan, China). All cell lines were cultured in DMEM or 1640 medium, contained 10 % fetal bovine serum (Gibco, USA) and 1 % penicillin/streptomycin in a humidified incubator (37 °C, 5 % CO2/95 % air).

2.2. CRISPR–Cas9 knockout system

We used the CRISPR–Cas9 editing system to knockout MYOF expression. In brief, we designed small guide RNAs (sgRNA) targeting human and mouse MYOF transcripts, cloned into the lentiCRISPRv2 vector (Plasmid #52961, Addgene). To generate lentiviral particles, 9 μg recombinant vector was co-transfected with 9ug pCMV-dR8.2 dvpr (Plasmid #8455, Addgene) and 0.9ug pCMV-VSV-G (Plasmid #8454, Addgene) into 1 × 107 HEK293T cells. Cell supernatants containing lentiviral particles were collected at 48 h after transfection and filtered through the sterile syringe filter (0.45 μm pore size, Millipore). PC cells were infected with prepared lentivirus and screened with 1 μg/mL puromycin for 2 weeks. To construct monoclonal cell lines, Flow cytometry was used to sort out individual cells and seed them in 96-well plates. The knockout efficiency of each monoclonal cell line was identified by Western blotting. All sgRNA sequences targeting MYOF are shown in Supplementary Table 1.

2.3. Short hairpin **RNA**, shRNA, plasmid and lentivirus construction, and transfection protocol

Overexpression vectors for human LCN2 and ILF3 genes and mouse LCN2 gene were synthesized by Genechem (Shanghai, China) and ligated into the lentiviral vector GV394, GV141 and GV127, respectively. To knock down human OTUB1, LCN2 and ILF3 genes, we screened hairpin shRNAs, which were synthesized by Genechem (Shanghai, China) and cloned into the lentiviral vector GV493. Lentiviral particles were produced using the packaging plasmids pHelper 1.0 and pHelper 2.0 (Genechem, Shanghai, China). To construct stably infected cells, transfected cells were cultured with medium containing 1 μg/mL puromycin for 2 weeks.

2.4. Transwell assay

Transwell membranes (Corning, NY, USA) with a pore size of 8 μm were used for the cell migration assay. A total of 200 μl serum-free medium ($5x10^5$ cells/ml) was added to the upper chamber, whereas 700ul medium containing 10 % FBS was added to the lower chamber. After 24 h of incubation, the chambers were washed with PBS, fixed with 4 % paraformaldehyde and stained with crystal violet. The adherent cells in the upper chamber were removed and the migrated cells in the lower chamber were counted under a microscope.

2.5. RNA isolation and RT-qPCR

The mRNA in cells was isolated and purified using FastPure Cell/Tissue Total RNA Isolation Kit V2 (Vazyme Biotech Co., Ltd). cDNA was synthesized with a RevertAid First Strand cDNA Synthesis Kit (Thermo Scientific). qPCR was performed with PowerUp SYBR Green Master Mix (Thermo Fisher) on LightCycler 96 Instrument (Roche). Relative expression was calculated using the 2-ΔΔCt method and normalized by the expression level of Actb. All primers were shown in Supplementary Table 2.

2.6. Western blot (WB) analysis

Cells were lysed using RIPA buffer containing protease inhibitors. Protein extracts were electrophoretically separated by 10 % SDS-PAGE gels and transferred to polyvinylidene fluoride membranes. After sealing with 5 % skimmed milk, the membrane was incubated with primary antibody at 4 °C overnight. The membrane was washed with TBST and then incubated with secondary antibody for 2 h at room temperature. Finally, protein bands were exposed using enhanced chemiluminescence. Antibodies used for Western blotting are listed in Supplementary Table 3.

2.7. Cell proliferation

To assess the proliferative capacity of the transfected cells, we used the MTS method (Promega) according to the manufacturer's manual. Cells were seeded at 800 per null in 96-well plates for 7 days. At each 24 h intervals, 20 μL of MTS reagent was added to each well and incubated at 37 °C for 4 h. The absorbance of the samples was measured at 490 nm using a microplate reader.

2.8. Soft agar assay

The experiment involved mixing tumor cells (3 × 103 per well) with 0.375 % Agarose and incubating them on six-well plates containing solidified 0.75 % Agarose (Thermo Fisher Scientific, Inc.) for 30 days. The cellular colonies were then counted under a microscope.

2.9. Cell cycle assay

Cells were collected, washed with PBS and fixed in 70 % ethanol. Cell cycle assay was detected by the Cell Cycle Analysis Kit (no. C1052; Beyotime, Shanghai, China). Cells were incubated with propidium iodide staining for 30 min. The DNA content was detected by BD FACSCalibur. The proportions of G1, S and G2/M phase cell populations were identified using ModFIT software.

2.10. mRNA stability analysis

MYOF knockout and control PC cells were treated with actinomycin D (5 μg/mL). At 0, 3, 6, 9 and 12 h of treatment, Trizol RNA was harvested and extracted for RT-qPCR analysis. The mRNA level at 0 time point was used as a control and the change in mRNA at different time points was calculated.

2.11. Immunoprecipitation (IP) and Co-immunoprecipitation (coIP)

PC cells were harvested and lysed in RIPA buffer containing protease inhibitors. Cell extracts were pre-purified with Protein A/G beads. Immunoprecipitation was performed with 2 μg of antibodies against MYOF, OTUB1 or ILF3 overnight at 4 °C, followed by incubation with Protein A/G beads for 2.5 h at 4 °C. The precipitated protein mixture was washed three times and subjected to LC-MS/MS analysis or immunoblotting.

2.12. Determination of MDA and GSH content

The intracellular glutathione (GSH) concentrations were determined using a biochemical assay kit (E-BC-K030-S, Elabscience), following the instructions provided by the manufacturer. Similarly, the concentration of malondialdehyde (MDA) in the cells was measured utilizing the MDA assay kit (E-BC-K025-S, Elabscience), following the manufacturer's protocol. The absorbance value of each index was detected by enzyme marker and the content in the cells was calculated.

2.13. GSH and oxidized GSH (GSSG) assay

The experiment employed the GSH and GSSG Assay Kit (Beyotime, S0053), in strict accordance with the standardized protocol for the separate detection of oxidized and reduced glutathione.

2.14. BODIPY 581/591C11 assay

The experimental groups consisted of: the RSL3-treated group (exposed to 2 μM RSL3 for 6 h), the FER-1-pretreated group (pretreated with 1 μM FER-1 for 1 h followed by co-treatment with RSL3 for 6 h), and the vehicle control group (DMSO at a final concentration of <0.1 %). After treatment, live cells were incubated with 1 μM BODIPY 581/591C11 (Beyotime, S0043S) at 37 °C in the dark for 30 min, followed by three washes with PBS. The cells were fixed with 4 % paraformaldehyde (PFA) at room temperature for 10 min and washed three times with PBS. Nuclear staining was performed using 1 μg/mL DAPI (Beyotime, C1005) at 37 °C in the dark for 10 min. After PBS washes, the samples were mounted with an antifade mounting medium (Life Technologies, P36934), light-cured in the dark, and sequentially imaged using fluorescence microscopy.

2.15. Intracellular oxidation level

The intracellular oxidation levels were measured using the DCF-DA probe (2′,7′-dichlorofluorescin diacetate). Cells were seeded at a density of 5×10^5 cells/well and treated with 10 μM RSL3 for 3 h after attachment. Following digestion with 0.25 % trypsin and centrifugation at 1000 rpm for 5 min, intracellular oxidation was assessed using 10 μM DCF-DA (Beyotime, S0033) through 30-min dark incubation according to the protocol. Fluorescence intensity was measured using a flow cytometer (BD Biosciences; excitation/emission wavelengths: 488/525 nm). Each experiment was performed in triplicate. Fluorescence intensity was measured using a flow cytometer. Data were normalized to the highest oxidation value observed in the experimental groups (set as 100 %) and expressed as mean ± standard deviation (% of max). It should be noted that DCF-DA is a broad-spectrum indicator of intracellular oxidation (not a specific ROS detection probe), and its methodological limitations have been thoroughly elucidated in the study by Kalyanaraman et al. [15].

2.16. Bioinformatic analysis

Gene expression data and clinical data for pancreatic cancer were downloaded from Gene Expression Omnibus (GEO) datasets, including GSE16515, GSE62452, GSE62165, and GSE28735.

2.17. Immunohistochemistry

The collected tissue samples were immersed in 4 % paraformaldehyde and fixed for 48 h. After dehydration and paraffin embedding, the slices were cut into sections of 4 μm thickness. Paraffin sections were placed in a 60° oven to bake the slices for 60 min to dissolve the paraffin on the sections and hydrate them. Sections were immersed using 0.01 M sodium citrate buffer at pH 6.0 for antigenic repair during high-pressure thermal repair. Afterward, follow the instructions for the ready-to-use immunohistochemical ultrasensitive UltraSensitiveTM SP kit. The IHC kit (KIT-9730) was purchased from Maixin Biotechnologies (Fuzhou, China).

2.18. Protein-protein docking

To predict the direct binding model between the three protein molecules MYOF, OTUB1, and ILF3, we obtained their 3D spatial structures from the AlphaFold Protein Structure Database (https://alphafold.ebi.ac.uk/). After analysing the crystal structure of MYOF, OTUB1 and ILF3, we used computational protein docking to predict their most likely binding model. Similarly, we used the GRAMM online tool to predict the most likely binding complex model of MYOF, OTUB1 and ILF3. The interaction surfaces in the protein complexes were further analyzed using the PDBePISA online tool (https://www.ebi.ac.uk/msd-srv/prot_int/pistart.html), Finally, we performed conformational mapping and docking region analysis using PYMOL (https://pymol.org/).

2.19. Small molecule inhibitor screening

Anti-tumour compound libraries were downloaded from the Selleck website (https://www.selleck.cn/index.html), followed by the use of Open Bable software for file format conversion, AutoDock Vina version 1.5.6 software for batch molecular docking, and PyMOL software for compound visualisation.

2.20. RNA immunoprecipitation

RNA-protein complexes are released by lysing cells using a pre-chilled lysis buffer (containing PMSF and protease inhibitors) at 4 °C for 1–2 h, followed by centrifugation to collect the supernatant. Next, Protein A/G magnetic beads are resuspended, washed with RIP buffer, and then incubated with negative control IgG antibody, positive control antibody (anti-SnRNP70), or target antibody (anti-ILF3) at 4 °C for 6–8 h. The bead-antibody complexes are mixed with cell lysate and incubated overnight at 4 °C. After washing, RNA is extracted using the TRIZOL method: TRIZOL and chloroform are added, followed by centrifugation to collect the aqueous phase, and RNA is precipitated with ethanol, then dissolved in RNase-free water. The purified RNA can be analyzed by qPCR to detect specific RNAs (e.g., LCN2 and U6), and the relative enrichment is calculated to compare the target group with negative and positive controls. The entire process must be conducted in an RNase-free environment, and RNase inhibitors should be used to prevent RNA degradation.

2.21. Chromatin isolation by RNA purification

Crosslink the cells with 1 % formaldehyde solution for 10 min. After crosslinking, terminate the reaction with glycine and wash the cells three times with PBS. After removing the supernatant, store the cells at −80 °C or proceed directly to the experiment. Next, resuspend the crosslinked cell pellet in lysis buffer containing protease inhibitors and RNase inhibitors, then sonicate to fragment the chromatin into 100–500 bp pieces. After centrifugation, collect the supernatant. Take a portion of the sample for DNA extraction and assess chromatin fragmentation by 2 % gel electrophoresis to ensure fragment sizes are between 100 and 1000 bp. Then, design and synthesize biotinylated DNA probes

complementary to the target RNA sequence. Incubate the probes with the cell lysate at 37 °C for 4 h to allow hybridization between the probes and the target RNA. Pre-treat streptavidin magnetic beads, wash them, and incubate with the probe-lysate mixture at 37 °C for 30 min to capture the RNA-chromatin complexes. Incubate the beads with PK buffer and proteinase K at 65 °C to release RNA. Extract RNA using TRIZOL, precipitate with ethanol, and dissolve in RNase-free water for qPCR analysis. At the same time, incubate the beads with elution buffer, RNase A, and RNase H at 37 °C to release proteins. Afterward, add protein loading buffer, boil, and use the sample for WB or mass spectrometry analysis. Finally, use qPCR to detect the relative enrichment of RNA, calculate the capture efficiency of target RNA, and compare the differences between the target group and the negative control group. Probe and primer sequences used in CHIRP assays and qPCR validation were as follows: 6 LCN2-specific probes (P1–P6) were designed: P1: AGCTGCATGGGTGGCACTGT, P2: TGGGACAGGGAAGACGATGT, P3: CTCTTAATGTTGCCCAGCGT, P4: CAGCTCATAGATGGTGGCAT, P5: TTCTGCTGCAGAGGGACCTT, and P6: TAGGCCCAGCCACAGGAGAC. Three LacZ control probes served as negative controls: P1: CTGAATATCGACGGTTTCCA, P2: GCTGTATCGCTGGATCAAAT, and P3: GTCGTTTTACAACGTCGTGA. qPCR validation employed the following primer pairs: LCN2 (forward: TACACTGGTCGATTGGGACA; reverse: CAAGGAGCTGACTTCGGAAC) and GAPDH (forward: TCCATGGCACCGTCAAG; reverse: CAGCCTTCTCCATGGTGG) as the reference gene.

2.22. Animal studies

In subcutaneous tumour experiments, 2×10^6 PC cells infected with different lentiviruses were injected subcutaneously into 4-week-old female BALB/c nude and C57 mice. Tumour size was measured every three days, length and width were recorded, and tumour volume (length × width2/2) was calculated. After 4 weeks, the mice were sacrificed and the tumors were harvested and weighed. To assess the effect of Picroside II on tumour growth, nude mice were injected subcutaneously with 2×10^6 PANC-1 cells or SW1990 cells. When the tumors were approximately 3 × 3 mm in size, the mice were randomly divided into two groups of 5 mice each. The mice were treated with Picroside II (MCE MedChemExpress, # HY-N0408; 0.4 mg/kg, i.p.) three times a week for 1 month, while the control group was injected with the same amount of saline. At the end of treatment, the mice were sacrificed and the tumors removed and weighed for immunohistochemical staining or Western blotting studies. For the tail vein injection lung metastasis assay, 1×10^6 pc cells were resuspended in 100 μL PBS and then injected into the tail vein of 4-week-old mice. Mice were necropsied after approximately 8–12 weeks and lung tissue was isolated, photographed and stained with HE. All work with mice was approved by the Animal Experimentation Ethics Committee of Guangzhou Medical University and conducted according to its regulations.

2.23. Cellular thermal shift assay (CETSA)

In the CETSA assay, PANC-1 cells were treated with or without Picroside II (300 μM) for 3 h. After treatment, cells were washed three times with PBS and harvested. Cell precipitates after centrifugation were resuspended with PBS supplemented with 1 % PMSF (Sigma), suspended and heated at the indicated temperatures (37, 42, 47, 52, and 57 °C), then cooled for 3 min and freeze-thawed three times with liquid nitrogen. The lysate was centrifuged to separate the supernatant from the precipitate and the supernatant was analyzed by immunoblotting.

2.24. Statistic

Statistical analyses were performed using GraphPad Prism 9.0 (GraphPad Software Inc., CA, USA). Two-tailed Student's t-test was used to compare the two groups. Overall survival curves were plotted using the Kaplan-Meyer method and compared using the log-rank test. Differences were considered statistically significant at $P < 0.05$.

3. Results

3.1. MYOF is overexpressed in PDAC and associated with poor prognosis

To explore potential biomarkers and therapeutic targets in pancreatic cancer, we utilized the TCGA database and the CPTAC protein database. In these both databases, 320 differentially expressed genes were identified simultaneously at mRNA and protein levels (Fig. 1A and Fig. S1A). Among the differentially expressed genes, we focused on MYOF. Although the potential involvement of MYOF in PDAC has been previously reported, the mechanisms need be further elucidated and the translational implication of targeting MYOF strategy remains to be explored. As shown, compared to normal tissues, MYOF was significantly highly expressed in PDAC tissues at mRNA level analyzed from TCGA database and at protein level analyzed from CPTAC database (Fig. 1B). Consistently, four data cohorts from GEO database showed MYOF mRNA upregulation in PDAC (Fig. S1B). The MYOF mRNA and protein levels positively correlated with PDAC histological grades progression (Fig. 1C). Furthermore, MYOF expression was also analyzed in GSE165399 scRNA-seq (single-cell RNA sequencing) of PDAC. By characteristic canonical cell markers, ten major cell types were visualized using t-Distributed Stochastic Neighbor Embedding (tSNE), classified as acinar cell, B cell, ductal cell, endothelial cell, fibroblast, malignant cell, myeloid cell, plasma cell, stellate cell and T cell (Fig. 1D). As shown, MYOF was mainly highly expressed in malignant cells (Fig. 1E). The MYOF protein levels in PDAC tissues were higher than that in paracancerous tissues (Fig. 1F). Compared to normal pancreatic ductal epithelial cells, the high expression of MYOF in PDAC cell lines was also confirmed (Fig. 1G). Additionally, MYOF protein not only located at lysosomes and proteasomes, but also scattered throughout the cytoplasm in PDAC tissues (Fig. 1H and I) and cell lines (Fig. 1J, K and Fig. S1C and D). Importantly, the clinical data analysis of PDAC from TCGA revealed that patients with higher MYOF expression had a poorer prognosis represented as disease free survival and overall survival (Fig. 1L). We observed that MYOF is overexpressed in PDAC tissues and cell lines, and its expression is associated with poor prognosis, consistent with previous findings [11].These results suggest the potential involvement of MYOF in PDAC development and progression.

3.2. MYOF promotes PDAC progression

To evaluate the biological functions of MYOF on the malignant phenotype of PDAC, we established stable MYOF knockout cell lines using CRISPR-Cas9 system (Fig. 2A). The cell proliferation was monitored using MTS assays. As shown, MYOF knockout decreased the proliferation ability of PDAC cells (Fig. 2B–G and Fig. S2A). The plat colony-forming assay and soft-agar colony-forming assay also showed that MYOF knockout significantly inhibited the colony-formation ability of PDAC cells (Fig. 2C, D and Fig. S2B and C). Thus, the effect of MYOF on cell cycle progression was examined. MYOF knockout resulted in increase in G0/G1 phase but decrease in G2/M phase (Fig. 2E and Fig. S2D). To investigate the effect of MYOF knockout on the invasion of PDAC cells, we conducted the transwell assay and indicated that MYOF knockout suppressed the invasive ability of PDAC cells (Fig. 2F and Fig. S2E). The inhibitory function of MYOF knockout on proliferation, cell cycle progression and invasion were confirmed in a mouse PDAC cell line Panc02 (Fig. 2G–J and Fig. S2F).

Then, to validate the oncogenic function of MYOF in PDAC cells in vivo, we established a sub-cutaneous xenograft assay and a lung metastasis model using human and mouse PDAC cell lines with MYOF knockout, respectively. MYOF knockout repressed tumor volume growth and tumor weight growth in nude mouse (Fig. 2K and L). MYOF knockout downregulated ki67 level in xenograft that representing as

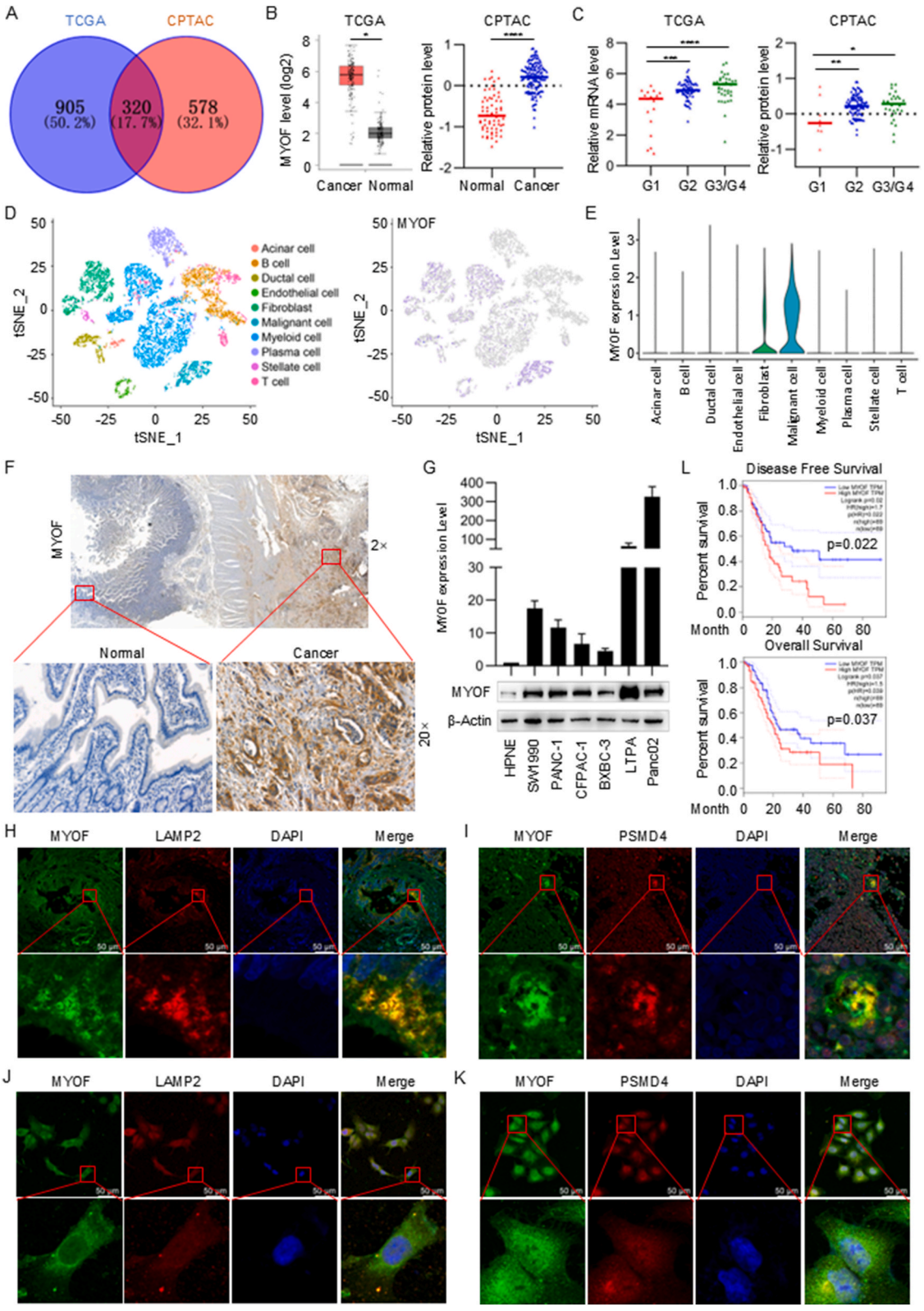

Fig. 1. MYOF is up-regulated in PDAC tissues and is associated with a poor prognosis. **A** Venn diagram of TCGA and CPTAC dataset showing 320 co-upregulated gene. **B** The expression of MYOF in TCGA-PAAD dataset and CPTAC-PDAC dataset. **C** In the TCGA and CPTAC database, the expression of MYOF in pancreatic cancer histological grades G2, G3 and G4 was higher than that in G1, and the difference was statistically significant. **D** The tSNE mapping of MYOF in different cellular taxa based on the public single-cell dataset GSE165399. **E** Violin plot of MYOF distribution across cellular subpopulations. **F** IHC staining was performed using an antibody against MYOF and representative photographs of MYOF in PDAC patients. **G** MYOF protein and mRNA expression levels in a normal pancreatic cell line and PC cell lines. **H** Immunofluorescence between MYOF (red) and LAMP2 (green) in pancreatic cancer tissue. **I** Immunofluorescence between MYOF (green) and PSMD4 (red) in pancreatic cancer tissue. **J** Immunofluorescence between MYOF (red) and LAMP2 (green) in pancreatic cancer cell line SW1990. **K** Immunofluorescence between MYOF (red) and PSMD4 (green) in pancreatic cancer cell line SW1990. **L** The overall survival and the disease-free survival of PDAC patient in MYOF-low or MYOF-high expression group. *$p < 0.05$, **$p < 0.01$, ***$p < 0.001$, ****$p < 0.001$.

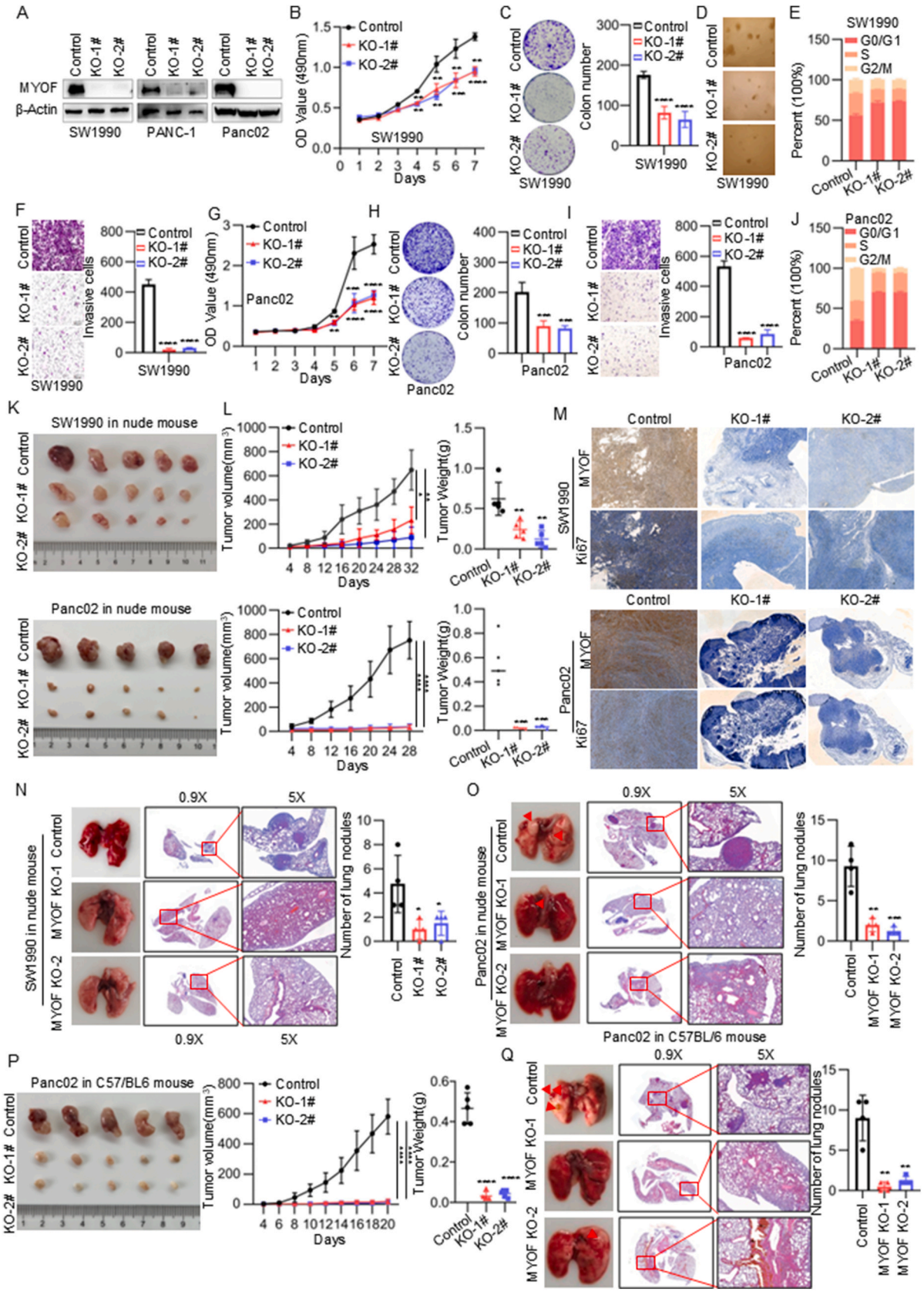

(caption on next page)

Fig. 2. MYOF promotes PDAC progression. **A** Western blot analysis of SW1990 PANC-1 and Panc02 stably transfected with MYOF knockdout lentiviruses and control lentiviruses. Total β-actin was used as a loading control. **B** The proliferation rate of SW1990 measured by MTS assay. **C** The colony formation assay. Left panel: representative images, right panel: quantification analysis. **D** Soft agar assays of PDAC cells. **E** Cell cycle changes were demonstrated by flow cytometry in SW1990 cell lines following the knockout of MYOF. **F** Transwell migration assays were performed to assess migration ability of MYOF-knockout stable cell lines. Representative images (left panel) and quantification (right panel) are shown as indicated. Data from independent experiments are presented as the mean ± SD. **G** The proliferation rate of Panc02 measured by MTS assay. **H** The colony formation assay. Left panel: representative images, right panel: quantification analysis. **I** Transwell migration assays. **J** Cell cycle assay. **K** Images of subcutaneous xenografts from mice in the MYOF KO and NC groups. n = 5. **L** Tumor volume growth curve and tumor weight scatter plot of subcutaneous xenograft. **M** The IHC staining of Ki67, MYOF in xenografted tumors. **N** Left: corresponding images of the lungs after injection of SW1990 cells by tail vein; images taken 10 weeks after injection. Right: statistical significance of the metastasis nodules number assessed by paired *t*-test. **O** Left: corresponding images of the lungs after injection of Panc02 cells by tail vein; images taken 3 months after injection. Right: statistical significance of the metastasis nodules number assessed by paired *t*-test. **P** The xenografted PDAC tumors in C57BL/6 mice. n = 5; The tumor volume quantification; The tumor weight quantification. **Q** Left: corresponding images of the lungs after injection of Panc02 cells by tail vein; images taken 3 months after injection. Right: statistical significance of the metastasis nodules number assessed by paired *t*-test. *p < 0.05, **p < 0.01, ***p < 0.001, ****p < 0.0001.

proliferation marker (Fig. 2M). Similarly, in the lung metastasis model, MYOF deletion significantly reduced the lung metastasis ability of human PDAC cells in nude mouse (Fig. 2N and O). Additionally, another model using immunocompetent C57BL/6 mouse was applied to monitor the tumor growth and metastasis ability mediated by MYOF in vivo. The suppressive effect of MYOF knockout on tumor growth and metastasis in vivo was further confirmed in the immunocompetent model (Fig. 2P and Q). These in vitro and in vivo data suggest the oncogenic role of MYOF in PDAC.

3.3. MYOF knockout induces ferroptosis in PDAC cells

To explore the molecular mechanisms underlying the oncogenic function of MYOF in PDAC, we performed transcriptome sequencing to identify differentially expressed genes in PDAC cells with MYOF knockout. There were 860 genes downregulated and 2018 genes upregulated in PDAC cells with MYOF knockout (Fig. S3A). The GO analysis showed that the biological process enrichment terms of downregulated DEGs by MYOF knockout were mainly associated with metabolic process (Fig. 3A and Fig. S3B). Further GO analysis of molecular function enrichment terms showed the DEGs were also associated with protein binding, catalytic activity, cation binding and metal ion binding (Fig. 3B and Fig. S3C). Because GO analysis DEGs mediated by MYOF knockout were involved in regulation of metabolic process and cation and metal ion binding, we wondered whether MYOF was involved in ferroptosis. Interestingly, Transmission electron microscopy (TME) analysis strongly indicated that MYOF knockout promoted mitochondria shrunk with elevated membrane density, a typical morphologic feature of ferroptosis. Thus, MYOF knockout induced ferroptosis in PDAC cells, and especially enhanced the effect of ferroptosis inducer RSL3 treatment (Fig. 3C). Additionally, a series of ferroptosis indicators were examined. MYOF knockout notably elevated the MDA and cellular oxidation levels but decreased the levels of GSH and ratio of GSH/GSSG in PDAC cells (Fig. 3D and Fig. S3D–E). Since lipid peroxidation is a key feature of ferroptosis, we stained the cells with BODIPY 581/591C11. MYOF knockout significantly increased lipid peroxidation induced by RSL3 (Fig. 3E–F and Fig. S3F). These results suggest MYOF knockout suppresses PDAC progression maybe via inducing ferroptosis.

3.4. MYOF knockout exerts effects via inhibiting LCN2 expression in PDAC cells

As shown above, MYOF knockout induced ferroptosis and MYOF-regulated DEGs were involved in metastatic process and metal ion binding. Among the DEGs, we focused on LCN2 due to its downregulation by MYOF knockout in PDAC cells. LCN2 also known as neutrophil gelatinase associated lipocalin (NGAL) is an iron-binding protein acting as a key suppressor of ferroptosis [16,17]. Here, the expression of LCN2 was significantly decreased at both mRNA and protein levels upon MYOF knockout (Fig. 4A). MYOF knockout resulting into LCN2 downregulation was also validated in xenograft tissues in nude mice (Fig. 4B). To determine the oncogenic function of LCN2 in PDAC, we constructed LCN2 knockdown in PDAC cells (Fig. S4A). Similar to MYOF knockout, LCN2 knockdown effectively inhibited the proliferative ability by MTS assay (Fig. S4B) and colon-formation assay (Fig. S4C) and invasive capacity (Fig. S4D) and induced G0/G1 phase arrest (Fig. S4E) in PDAC cells. Then, whether LCN2 was involved in ferroptosis of PDAC cells was determined. Transmission electron microscopy (TME) analysis revealed that LCN2 knockdown promoted mitochondria shrunk with elevated membrane density (Fig. S4F). LCN2 knockdown notably elevated the MDA and Cellular oxidation levels but decreased the levels of GSH and the ratio of GSH/GSSG in PDAC cells (Fig. S4G). LCN2 knockdown significantly increased lipid peroxidation induced by RSL3 (Fig. S4H–I). We then performed rescue experiments to determine whether the pro-tumorigenic effect of MYOF in PDAC is dependent on LCN2 expression. LCN2 was overexpressed in PDAC cells with MYOF knockout (Fig. 4C, Fig. S4J). LCN2 overexpression reversed the inhibitive effect of MYOF knockout on proliferation (Fig. 4D and E) and invasion ability (Fig. 4F) and cell cycle arrest (Fig. 4G) in human PDAC cells. The function of LCN2 was also validated in mouse PDAC cells (Fig. S4K–N). Moreover, overexpression of LCN2 reversed the ferroptosis characteristics induced by MYOF knockout both in human and mouse PDAC cells (Fig. 4H–I, Fig.S4O-Q). Expectedly, LCN2 overexpression also disrupted the in vivo tumor growth of PDAC mediated by MYOF knockout (Fig. 4J). Additionally, ectopic LCN2 expression also led to xenograft regrowth of mouse PDAC cells with MYOF knockout in immunocompetent C57BL/6 mouse (Fig. S4R–S). These results suggest MYOF exerts its tumor promotive role via preventing ferroptosis by upregulating LCN2 expression.

3.5. MYOF maintains LCN2 mRNA stability via ILF3 in PDAC cells

To investigate whether MYOF regulates LCN2 mRNA expression at transcriptional level or at post-transcriptional level, the actinomycin D was used to block de novo transcription. Under actinomycin D treatment, MYOF knockout still led to LCN2 mRNA decrease (Fig. 5A and Fig. S5A). To identify factors involved in LCN2 mRNA stability, first the potential RNA binding proteins (RBPs) targeting LCN2 mRNA were predicted using the online software (RBPsuite) and 223 RBPs were predicted (Fig. S5B). Then, MYOF protein was immunopurified in PDAC cells, followed by tandem-mass-tag mass spectrometry analysis (IP-MS) to identify MYOF-interacted proteins (Fig. 5B). There were 128 proteins potentially interacting with MYOF in PDAC cells were identified (Supplementary Table S4). Further analysis showed six proteins were identified in both bioinformatics prediction data and IP-MS data (Fig. 5C). Among the six proteins, we focused on IFL3 that is a well-known RNA binding protein maintaining mRNA stability. The binding between LCN2 mRNA and ILF3 protein was predicted using the online software (RBPsuite) (Fig. 5D). Further analysis showed ILF3 expression was positively correlated with LCN2 expression in PDAC (Fig. S5C). We employed RNA immunoprecipitation (RIP) combined with RT-qPCR, using IgG antibody as negative control and SnRNP70 as positive control, to successfully validate the specific binding between ILF3 protein and LCN2 mRNA in PDAC cells (Fig. 5E). To further confirm this

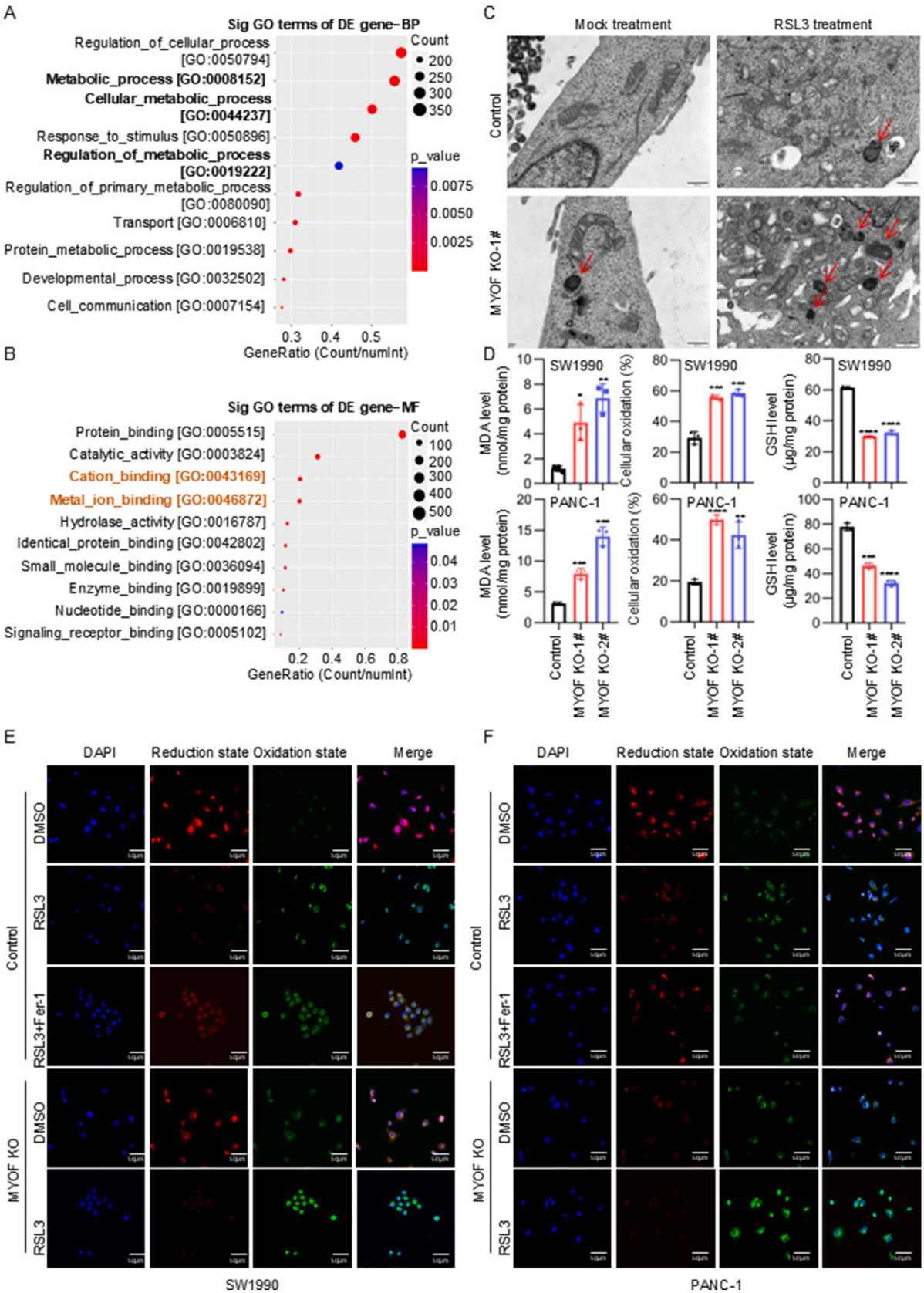

Fig. 3. MYOF knockout induces ferroptosis in PDAC cells. **A** GO enrichment analysis was performed to predict the downstream biological processes of MYOF. **B** GO enrichment analysis was performed to predict the downstream molecular function of MYOF. **C** Transmission electron microscopy images. **D** Levels of malondialdehyde (MDA), cellular oxidation (%) and glutathione (GSH) in control and MYOF knockout PDAC cells. n = 3. **E-F** The confocal laser scanning microscopy images of C11-BODIPY581/591-stained SW1990 and PANC-1 cells after treatment with different formulations. Scale bar = 50 μm *p < 0.05, **p < 0.01, ***p < 0.001, ****p < 0.0001.

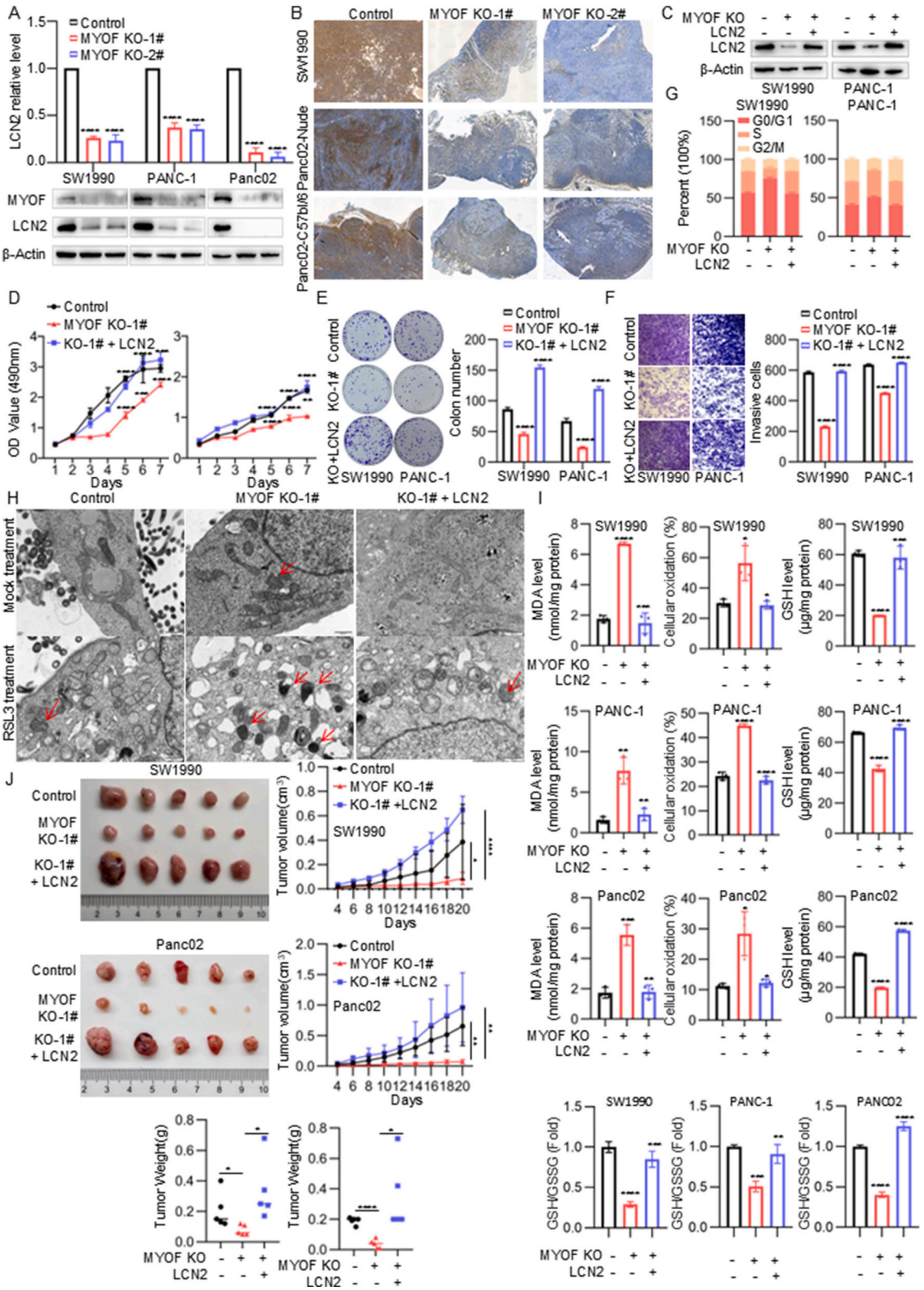

Fig. 4. MYOF knockout exerts effects via inhibiting LCN2 epxression in PDAC cells. **A** Gene abundance and protein levels of LCN2 after knockdown of MYOF. **B** The IHC staining of LCN2 in xenografted tumors. **C** Western blot analysis of LCN2 overexpression in stable knockout MYOF cell lines. **D** The proliferation rate of PDAC cells measured by MTS assay. **E** The colony formation assay. Left panel: representative images, right panel: quantification analysis. **F** Transwell migration assays. **G** Cell cycle assay. **H** Transmission electron microscopy images. **I** Malondialdehyde (MDA), cellular oxidation (%), Glutathione (GSH) levels and Ratio of GSH/GSSG in cells. n = 3. **J** Images of subcutaneous xenografts from Nude mice. n = 5; Tumor volume growth curves; Tumor weight scatter plot for subcutaneous xenografts. *p < 0.05, **p < 0.01, ***p < 0.001, ****p < 0.0001.

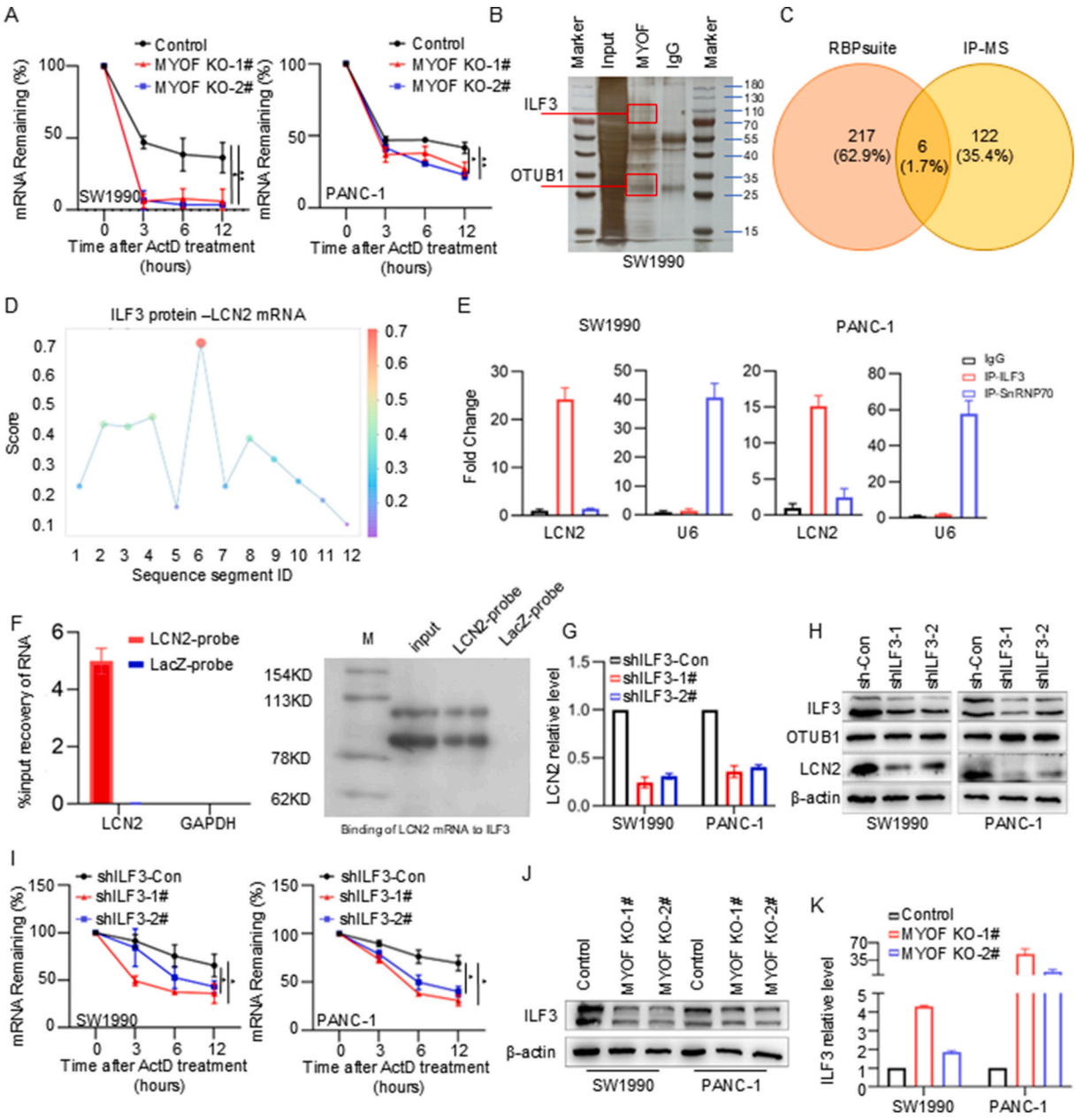

Fig. 5. MYOF knockout exerts effects via inhibiting LCN2 epxression in PDAC cells. **A** RT-PCR of LCN2 in PDAC cells from MYOF-knockout group and control groups by actinomycin D treatment (5 μg/mL) over time. **B** Silver staining of IP cell lysates. **C** Wayne diagram of RBPs and MYOF-interacting proteins; **D** Fold-out plots showing the binding scores of ILF3 protein to each fragment of LCN2 mRNA. **E** Research reveals that ILF3 interacts with LCN2 mRNA, as evidenced by RNA immunoprecipitation (RIP) experiments conducted in SW1990 and PANC-1 cells. Anti-ILF3 antibodies were employed for targeted detection, while anti-SNRNP70 (positive control) and anti-IgG (negative control) were used as comparative controls. Following this, RT-qPCR was carried out with primers designed for the specific mRNA. The relative enrichment of RIP-isolated mRNA compared to input samples was quantified, with outcomes expressed as mean ± SD. **F** Through ChIRP experiments, the enrichment of LCN2 mRNA and the pull-down efficiency of ILF3 protein in SW1990 cells were detected using an LCN2-targeting probe compared to a negative control LacZ probe. **G** QRCR to verify the transcript levels of LCN2 after interference with ILF3. **H** WB to verify the expression of relevant genes after interference with ILF3 in pancreatic cancer cell lines. **I** RT-PCR results of LCN2 changes over time in PDAC cells before and after interference with ILF3 by actinomycin D treatment (10 μg/mL). Data were expressed as mean ± SD. **J, K** WB and qPCR verified the transcription and translation levels of ILF3 after MYOF knockout. *$p < 0.05$, **$p < 0.01$, ***$p < 0.001$, ****$p < 0.0001$.

interaction, we obtained mutually corroborative results through chromatin isolation by RNA purification (ChIRP) assay and WB analysis (Fig. 5F). The ChIRP experiments conducted in SW1990 cell line demonstrated that, compared with the negative control LacZ probe, the LCN2-specific probe could significantly enrich LCN2 mRNA ($p < 0.01$) and selectively capture ILF3 protein. WB analysis further confirmed the existence of this specific interaction. These results consistently demonstrate from multiple experimental perspectives that LCN2 mRNA and ILF3 protein form stable RNA-protein complexes in PDAC cells. Interestingly, ILF3 knockdown downregulated LCN2 mRNA and protein level (Fig. 5G and H) and also decreased LCN2 mRNA stability (Fig. 5I). Expectedly, MYOF knockout led to decrease of ILF3 at protein level (Fig. 5J and Fig. S5D). Whereas, MYOF knockout even increased ILF3 mRNA level in PDAC cells (Fig. 5K and Fig. S5E) implying negative feedback regulation due to protein decrease. Additionally, MYOF knockout resulting into decrease of ILF3 protein level was also validated

in xenograft tissues in nude mice (Fig. 5L and Fig. S5F). These results suggest that MYOF maintains ILF3 protein stability which hence maintains LCN2 mRNA stability in PDAC cells.

3.6. MYOF recruits OTUB1 to inhibit ILF3 ubiquitination degradation

Given that MYOF knockout decreased ILF3 expression at protein level but even increased at mRNA level, we wondered to explore how MYOF maintains ILF3 protein level in PDAC cells. After treating the PDAC cells with cycloheximide (CHX) which blocked the protein synthesis to study the effect of MYOF on ILF3 protein turnover, we found that MYOF knockout significantly reduced the half-life of ILF3 protein in PDAC cells (Fig. 6A and Fig. S6A). On the other hand, the decrease in ILF3 protein caused by MYOF knockout was reversed by treatment of the proteasome inhibitor, MG132 (Fig. 6B and Fig. S6B). MYOF knockout enhanced the ubiquitination level of ILF3 protein, indicating MYOF promoted deubiquitination of ILF3 protein in PDAC cells (Fig. 6C). Thus, we wondered how MYOF regulates ubiquitination modification of ILF3 protein. MYOF protein was immunoprecipitated from PDAC cells (Fig. 5B) and the interacting proteins with MYOF were analyzed using mass spectrometry (Supplementary Table S4). Among the potential proteins, except ILF3, we focused on OTUB1 which acts as a deubiquitinating enzyme. Then, the ILF3 and OTUB1 protein were detected in the immunoprecipitation with MYOF antibody, indicating the association between MYOF and ILF3 and between MYOF and OTUB1 (Fig. 6D). To wonder whether MYOF mediated the interaction between ILF3 and OTUB1, first the protein structure (Fig. S6B) and the association between these three proteins were predicted by online software. The predicted interaction free energy between proteins indicated the potential direct interaction between MYOF and OTUB1 and between MYOF and ILF3, but not between OTUB1 and ILF3 (Fig. 6E and Fig. S6D). LIGPLOT was used to map the “eyelash figure” of protein-protein interactions (Fig. S6E), showing the potential binding domains between MYOF, OTUB1 and ILF3.Then, the immunoprecipitation was performed in PDAC cells with MYOF knockout or negative control. The reciprocal co-immunoprecipitation showed strong association between ILF3 and OTUB1 in PDAC cells, but MYOF knockout weakened this association (Fig. 6F). Furthermore, OTUB1 knockdown decreased ILF3 protein level accompanied with decrease of LCN2 expression (Fig. 6G). After treating the PDAC cells with cycloheximide (CHX) which blocked the protein synthesis to study the effect of OTUB1 on ILF3 protein turnover, we found that OTUB1 knockdown significantly reduced the half-life of ILF3 protein in PDAC cells (Fig. 6H). OTUB1 knockdown enhanced the ubiquitination of ILF3 protein in PDAC cells (Fig. 6I). To elucidate the role of OTUB1 in pancreatic ductal adenocarcinoma (PDAC), we knocked down the expression level of OTUB1 in both the control and MYOF knockout groups (Fig. 6J). We found that knocking down OTUB1 in the control group caused a significantly larger change in ILF3 ubiquitination levels compared to the changes observed in the MYOF knockout group (Fig. 6K). Additionally, knocking down OTUB1 in the control group had a significantly stronger inhibitory effect on tumor growth compared to the effects observed in the MYOF knockout group. These results suggest that MYOF acts as a scaffold to prevent ILF3 ubiquitination degradation by OTUB1 in PDAC cells.

3.7. Targeting MYOF by picroside II suppresses PDAC progression

Because of the critical function of MYOF in PDAC progression, here we used Autodock software for batch screening of small molecule inhibitors from the Anti-tumour Compound Library (https://www.selleck.cn/index.html). Later, based on the analysis of binding energy and number of hydrogen bonds binding, the binding between Picroside II (P-II) and MYOF protein was visualized by PyMOL software (Fig. 7A). The cellular thermal shift assay (CETSA) as a method to assess the binding affinity of drugs to targeted proteins in cells based on thermal stabilization of target proteins after binding by their ligands, was performed to validate the direct binding of P-II to MYOF in PDAC cells. PDAC cells treated with P-II were collected, lysed and heated. In comparison with the control treatment, P-II treatment led to a markedly increased thermal stability of MYOF protein at different temperatures (Fig. 7B). Then, a series of experiments were employed to validate the effect of P-II on PDAC cells. P-II treatment effectively inhibited the proliferation ability (Fig. 7C) and invasion (Fig. 7D) in vitro. P-II treatment also inhibited PDAC tumor growth in vivo (Fig. 7E and F). Then, the effect of P-II on MYOF protein was determined. P-II treatment decreased protein levels of MYOF and its downstream effector ILF3 and LCN2, but not its partner OTUB1 (Fig. 7G). Moreover, Bafa1 but not MG132 treatment could reverse picroside II treatment induced MYOF decrease (Fig. 7H). Moreover, Bafa1 but not MG132 treatment could reverse picroside II treatment-induced MYOF decrease (Fig. 7H). This suggests that the reduction in MYOF protein levels induced by picroside II is likely mediated through autophagy rather than the proteasome degradation pathway, as Bafa1 (an autophagy inhibitor) effectively reversed the decrease, while MG132 (a proteasome inhibitor) did not show a similar effect. Transmission electron microscopy (TEM) analysis revealed that P-II promotes mitochondrial contraction and enhances membrane density, additionally boosting the effectiveness of the ferroptosis inducer RSL3 (Fig. S7A). P-II significantly increases the levels of malondialdehyde (MDA) and cellular oxidation in PDAC cells, while concurrently decreasing the levels of GSH and the ratio of GSH/GSSG (Fig. S7B). P-II significantly increased lipid peroxidation induced by RSL3 (Fig. S7C–D). These results suggest Picroside II would be a potential MYOF inhibitor suppressing PDAC progression.

4. Discussion

In this study, we confirmed MYOF overexpression in PDAC using a series of online datasheet and found that MYOF deletion inhibited PDAC progression. MYOF knockout induced ferroptosis via downregulating LCN2 mRNA level post-transcriptionally. Moreover, MYOF acts as a molecular scaffold to mediate the indirect association between ILF3 and OTUB1, resulting into inhibition of ILF3 protein degradation. ILF3 binds to LCN2 mRNA and maintains its mRNA stability. Importantly, we screened and identified compound Picroside II potentially targeted MYOF to suppress PDAC progression. Our study yields several new insights in the role and mechanism of MYOF in PDAC and provides a novel therapy strategy by targeting MYOF.

First, MYOF overexpression in PDAC was confirmed by bioinformatics analysis and experimental validation. MYOF has been demonstrated to play a critical role in maintaining lysosomal integrity in PDAC, protecting cells from membrane stress and supporting tumor growth [11]. However, upon detection in PDAC tissue samples and cell lines, MYOF protein was found to be scattered throughout the cytoplasm rather than limited to mitochondria or lysosome as reported [10,11]. This discovery prompts us to wonder if MYOF has additional functions and mechanisms. We further found that MYOF deletion inhibited PDAC progression in vitro and in vivo and induced ferroptosis. Mechanistically, MYOF acts as a molecular scaffold facilitating OTUB1-ILF3 interaction to prevent ILF3 ubiquitination and degradation, revealing its novel role in protein stability regulation. Given MYOF’s ability to maintain lysosomal integrity, its role in ferroptosis resistance may be attributed to its stabilization of lysosomal membranes, preventing the release of iron and cellular oxidation levels, which are key triggers of ferroptosis. In this study, MYOF knockout led to increased cellular oxidation levels and lipid peroxidation, further validating its association with ferroptosis. This suggests that MYOF’s lysosomal function not only supports nutrient recycling and tumor growth but also protects cells from ferroptosis by maintaining intracellular iron homeostasis and preventing oxidative stress. The dual regulatory capacity of MYOF in both lysosomal membrane repair and protein stability establishes an integrated mechanism driving PDAC progression and ferroptosis resistance.

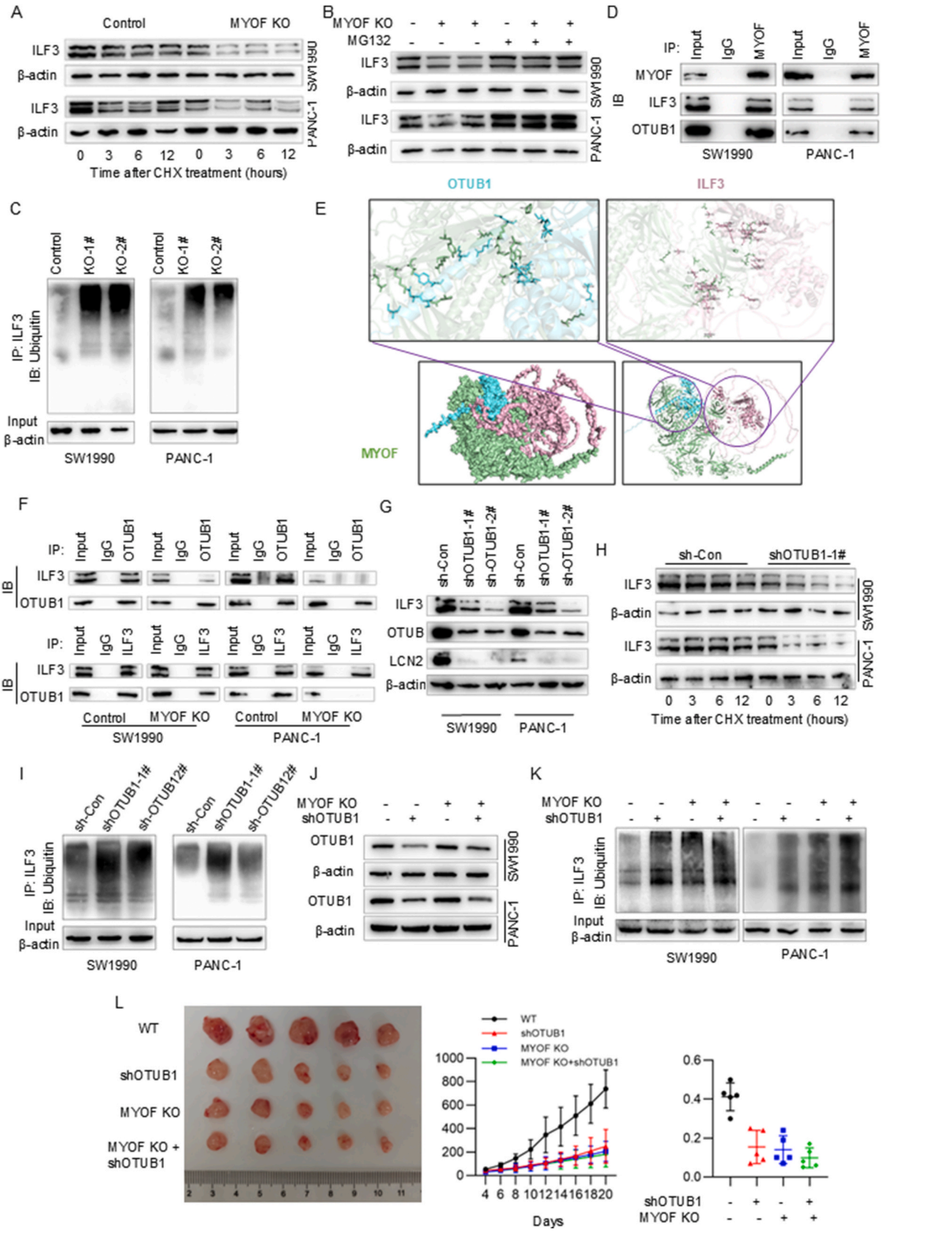

(caption on next page)

Fig. 6. MYOF recruits OTUB1 to inhibit ILF3 ubiquitination degradation. **A** Degradation of ILF3 protein was detected in PDAC cells after treatment of CHX at the indicated time points; **B** Western blot analysis of ILF3 expression after 6h treatment with 10 μM MG132; **C** ILF3 ubiquitylation was analyzed by immunoprecipitation using an anti-ILF3 antibody and immunoblotting was carried out with anti-Ub antibody; **D** Immunoprecipitation by using anti-MYOF antibody and immunoblotting with anti ILF3 and anti-OTUB1 antibodies; **E** Predicting binding complex models for MYOF, OTUB1 and ILF3 using the GRAMM online protein docking tool; **F** Immunoprecipitation was performed and detected by immunoblotting using anti-ILF3 or anti-OTUB1 antibodies; **G** After interfering with OTUB1, Western blot analysis of ILF3 expression after 6h treatment with 10 μM MG132. **H**. After interfering with OTUB1, degradation of ILF3 protein was detected after treatment of CHX at the indicated time points. **I** Cells from both the interfering OTUB1 and control groups were immunoprecipitated using an anti-ILF3 antibody. The resulting samples were analyzed for ILF3 ubiquitination and then immunoblotted with an anti-Ub antibody. **J** The Western blotting analysis identified the expression levels of OTUB1 in SW1990 and PANC-1 cells following OTUB1 knockdown. **K** The cells in each group were immunoprecipitated with anti-ILF3 antibody. The samples were then analyzed for ILF3 ubiquitination by Western blotting with anti-UB antibodies. **L** Images of subcutaneous xenografts from Nude mice. n = 5; Tumor volume growth curves; Tumor weight scatter plot for subcutaneous xenografts. *p < 0.05, **p < 0.01, ***p < 0.001, ****p < 0.0001.

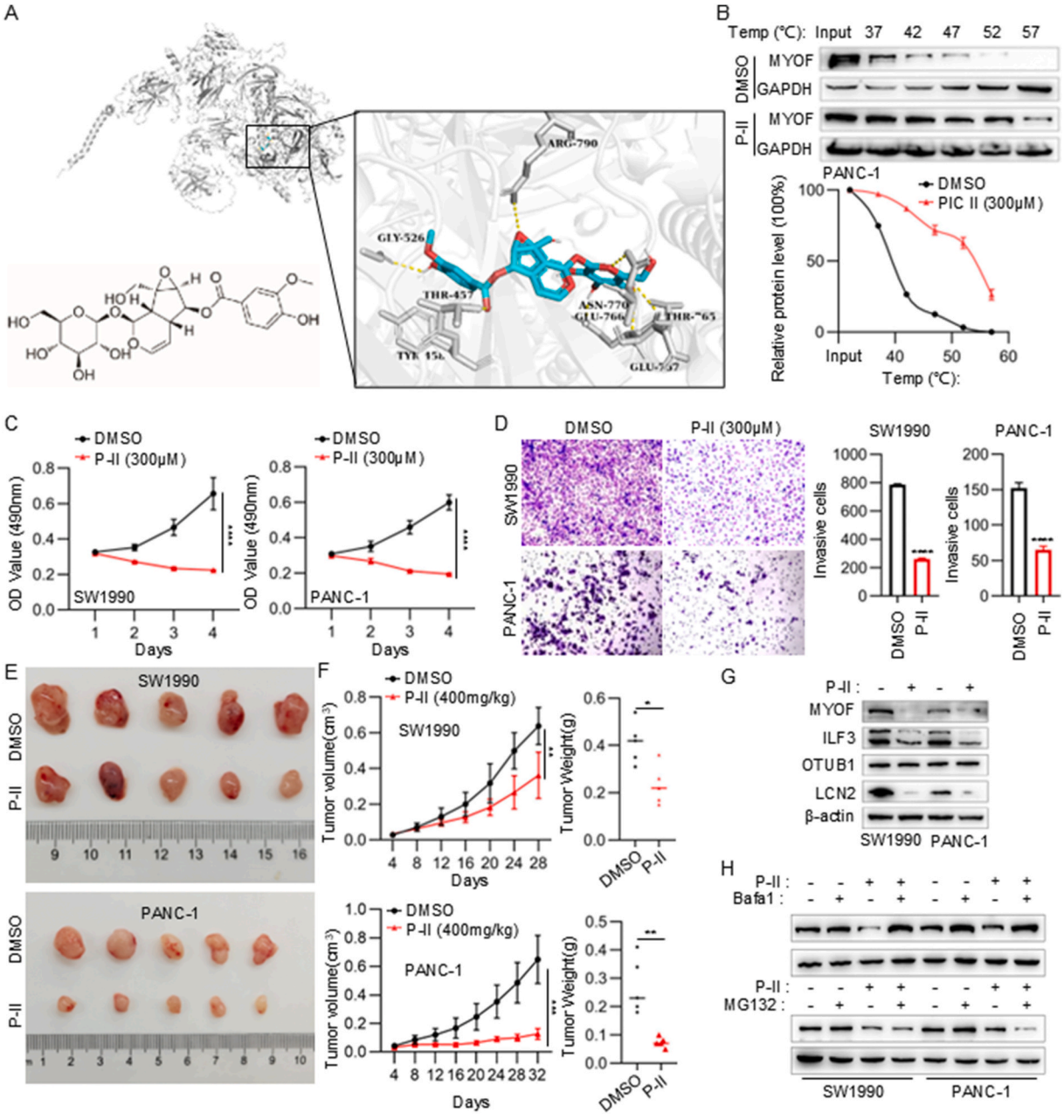

Fig. 7. Targeting MYOF by Picroside II suppresses PDAC progression. **A** AutoDock Vina software was applied to predict the molecular docking of MYOF with Picroside II; **B** The binding affinity of MYOF with Picroside II was evaluated and verified by the CETSA method, and the melting curves were fitted with Boltzmann stype GraphPad. **C** MTS proliferation assay to detect the proliferative ability of cells in Picroside II-treated and untreated groups; **D** Transwell migration assay. **E** Images of subcutaneous xenografts from mice in Picroside II-treated and untreated groups. **F** Tumour growth curves of mice in Picroside II-treated and untreated groups; Tumour weights of Picroside II-treated and untreated groups of mice. **G** Expression of MYOF, ILF3, OTUB1, LCN2 after Picroside II treatment. **H** WB assay to detect whether Bafa1 or MG132 can reverse Picroside II's effect on MYOF effect of Picroside II. *p < 0.05, **p < 0.01, ***p < 0.001, ****p < 0.0001.

Second, LCN2 also referred to as neutrophil gelatinase-associated lipocalin (NGAL), is a secreted glycoprotein initially identified in sequestering iron to combat bacterial infection by preventing bacterial iron acquisition [18]. LCN2, a key iron-binding protein, has been widely implicated in ferroptosis regulation across diverse disease models. Ferroptosis, characterized by iron-dependent lipid peroxidation, is modulated by LCN2 through its role in iron homeostasis and antioxidant defense. For instance, Liu et al. demonstrated that LCN2 depletion mimics NUPR1 deficiency in inducing ferroptosis [19], while its re-expression restores resistance to ferroptosis. Yao et al. further revealed that LIFR deficiency upregulates LCN2 via NF-κB activation [16], reducing sensitivity to ferroptosis inducers, whereas LCN2-neutralizing antibodies enhance sorafenib efficacy in hepatocellular carcinoma. Chaudhary et al. reported that LCN2 suppresses ferroptosis by reducing intracellular iron levels and stimulating glutathione peroxidase 4 (GPX4) and xCT expression [20]. Additionally, Jiang et al. highlighted HNRNPA2B1-mediated m6A modifications of FOXM1 as a mechanism to upregulate LCN2, conferring ferroptosis resistance in endometrial cancer [21]. These findings collectively underscore LCN2's dual role in iron sequestration and redox balance, positioning it as a critical regulator of ferroptosis and a potential therapeutic target in cancers, including PDAC. LCN2 is highly expressed in various cancer types and can confer cancer progression by promoting cancer cell survival, growth and metastasis. In colorectal cancer, high LCN2 expression is correlated with tumorigenesis and poor prognosis [22]. LCN2 interacted with and stabilizes integrin β3 protein to activate the SRC/AKT/ERK signaling mediating 5-fluorouracil resistance [23]. LCN2 was reported to be consistently linked with invasive breast cancer and poorer survival by inducing EMT (epithelial to mesenchymal transition) and maintaining poorly differentiated phenotype through the ERalpha/Slug axis [24]. LCN2 was also involved in SASP-induced breast cancer cells plasticity resulting in increased proliferation, migration and EMT, but decreased response to chemotherapy [25]. Additionally, cancer cells express LCN2 and its receptor SCL22A17 to promote leptomeningeal metastasis by iron-binding sequestration property [26]. LCN2 from granulocyte induced inflammatory activation of astrocytes, facilitating myeloid cell recruitment and cancer brain metastasis [27].

Third, LCN2 overexpression was mainly regulated by mRNA stability post-transcriptionally in PDAC cells. Unlike function exploration, the studies on regulation of LCN2 expression are still limited. In chemoresistant colorectal cancer cells LCN2 was upregulated by LCN2 promoter demethylation [23]. Here, we found MYOF knockout led to decreased stability of LCN2 mRNA via decrease of ILF3 protein. ILF3 (interleukin enhancer-binding factor 3), also referred as nuclear factor NF90/NF110, encodes a double-stranded RNA (dsRNA)-binding protein. ILF3 participates in diverse cellular functions such as mRNA stabilization, translation regulation and noncoding RNA biogenesis through binding to different cellular RNAs with other proteins [28]. ILF3 is highly expressed in a broad spectrum of cancer types. ILF3 has been reported to increase cyclin E1 mRNA stability to regulate the cell cycle of hepatocellular carcinoma cells [29] and to promote oral squamous cell carcinoma growth [30]. About the regulation of ILF3 itself, it has been reported that EGF-MEK-ERK pathway phosphorylated ILF3 to hinder E3 ligase speckle-type POZ protein (SPOP)-mediated ubiquitination and degradation [31]. In esophageal cancer, lncRNA MALR interacted with ILF3 and promoted ILF3 protein stability leading to HIF1α mRNA stability [32]. The regulation and function of ILF3 in cancer is emerging, but remains elusive.

Fourth, MYOF recruits OTUB1 to inhibit ubiquitination and degradation of ILF3 protein. Here, we found that MYOF knockout led to decrease of ILF3 expression at protein level but not mRNA level. MYOF deletion enhanced the ubiquitination of ILF3 protein. The MYOF interacting proteins involved in ILF3 ubiquitination was explored by CoIP-mass spectrometry analysis and OTUB1 was selected for further study. Ubiquitination is a post-translational modification of proteins that regulates their stability and degradation. Deubiquitinating enzymes belong to the proteasome superfamily. OTUB1 is a core member of the ovarian tumor domain protease (OUT) subfamily of deubiquitinases that blocks ubiquitination resulting into protein stability involved in many physiological and pathological processes [33]. OTUB1 as an oncogene stabilizes several critical oncoproteins to modulate tumorigenesis, invasion, metastasis and therapy response in multiple cancer types. OTUB1 deubiquitinates and stabilizes MYC protein contributing to HK2 mediated glycolysis and breast tumorigenesis [34], SLC7A11 and GPX4 proteins inhibiting ferroptosis and promoting cancer metastasis [35,36]. Disrupting the interaction of OTUB1 and c-Maf led to c-Maf degradation and c-Maf-expressing multiple myeloma cell apoptosis [37]. Here, we found OTUB1 enhanced ILF3 ubiquitination and degradation in PDAC cells. Our further findings suggested MYOF acts as a molecular scaffold to recruit both OTUB1 and ILF3 protein finally relieving ILF3 ubiquitination modification and subsequent LCN2 mRNA stability in PDAC cells.

Fifth, we screened a natural compound targeting MYOF to inhibited PDAC progression. Given the important function of MYOF in PDAC cells, targeting MYOF will provide a new strategy for PDAC treatment. Recently, the small molecule inhibitor targeting MYOF is being intently explored. Zhang et al. first reported WJ460 is a MYOF inhibitor that inhibits breast cancer progression in vivo model [38]. Due to poor metabolic stability and water solubility, based on WJ460 Gu et al. developed another MYOF inhibitor E4 with the water solubility improved by about 22-times than that of WJ460 [39]. It is well known that it will take a long period to develop a new protein targeting small molecule inhibitor with specific and effective druglike ability. Thus, we prompted to screen a MYOF targeting compound with druglike property and focused on Picroside II (P-II) because of its safety in clinical use. P-II is a flavonoid compound that extracted from the well-known traditional Chinese medicinal herb, Picrorhiza kurroa. This herb has been conventionally used for the treatment of liver and respiratory disorders, chronic fever and asthma [40,41]. P-II is one of the most effective components extracted from this herb. Many pharmacological effects of P-II have been reported, including hepatoprotective, anti-inflammatory and neuroprotective activities [42]. The anti-cancer effect of P-II is also emerging [43,44]. Here, we demonstrated P-II inhibited PDAC progression and identified P-II would bind to MYOF resulting into decrease of MYOF protein level and downstream signaling, suggesting P-II would target MYOF in PDAC cells. Although previous studies have shown that Picroside II has antioxidant activity [45,46], its mechanism of action in PDAC may be more complex. Our study found that Picroside II targets the MYOF protein, inducing its degradation via the autophagy pathway, thereby inhibiting PDAC progression. This mechanism of action does not contradict its traditional antioxidant activity; on the contrary, it may reflect the pleiotropic effects of Picroside II in different cellular environments. Notably, Picroside II treatment did increase oxidative stress in PDAC cells, which is consistent with the ferroptosis phenotype induced by MYOF knockout. This seemingly contradictory phenomenon may arise from the specific inhibitory effect of Picroside II on MYOF, leading to the downregulation of LCN2 expression, which in turn disrupts cellular iron homeostasis and the antioxidant defense system. This finding is consistent with the study by Hayes JD et al., which found that certain compounds can induce ferroptosis by targeting specific proteins, independent of their inherent antioxidant properties [47].Whereas, Bafa1 but not MG132 would reverse P-II induced MYOF protein decrease, implying P-II targets MYOF to autophagy mediated protein degradation. The detailed molecular mechanisms will be explored in our further studies.

In summary, our study indicates a new MYOF/OTUB1-ILF3/LCN2 signal pathway operated in PDAC. This signaling is essential for maintenance of aggressive behaviors of PDAC. Our study also identifies a natural compound P-II with druglike ability targeting MYOF exerting potential anti-cancer effect in PDAC.

CRediT authorship contribution statement

Zhihui Li: Writing – review & editing, Writing – original draft, Software, Resources, Project administration, Methodology, Investigation, Formal analysis, Data curation, Conceptualization. **Jianlei Zhang:** Writing – review & editing, Writing – original draft, Data curation, Conceptualization. **Jiang Yin:** Funding acquisition. **Wen Ma:** Resources. **Hongfan Liao:** Software. **Lv Ling:** Formal analysis. **Qingfeng Zou:** Funding acquisition. **Yabing Cao:** Supervision, Funding acquisition. **Ying Song:** Visualization. **Guopei Zheng:** Writing – original draft, Supervision, Funding acquisition. **Xiaoye Hu:** Methodology. **Guohua Yang:** Supervision. **Nan Li:** Writing – review & editing, Writing – original draft, Investigation.

Funding

This work was supported by National Natural Science Funds (81401989), Natural Science Foundation of Guangdong Province (2021A1515010988, 2023A1515030053), Educational Commission of Guangdong Province (2022ZDZX2049), Science and Technology Program of Guangzhou (2023A03J0429), and the Guangzhou Key Medical Discipline Construction Project Fund.

Declaration of competing interest

The authors declare that they have no known competing financial interests or personal relationships that could have appeared to influence the work reported in this paper.

Appendix A. Supplementary data

Supplementary data to this article can be found online at https://doi.org/10.1016/j.redox.2025.103665.

Data availability

No data was used for the research described in the article.

References

[1] H. Sung, et al., Global cancer statistics 2020: GLOBOCAN estimates of incidence and mortality worldwide for 36 cancers in 185 countries, CA Cancer J. Clin. 71 (2021) 209–249.
[2] L.D. Wood, M.I. Canto, E.M. Jaffee, D.M. Simeone, Pancreatic cancer: pathogenesis, screening, diagnosis, and treatment, Gastroenterology 163 (2022) 386–402, e381.
[3] J. Cai, et al., Advances in the epidemiology of pancreatic cancer: trends, risk factors, screening, and prognosis, Cancer Lett. 520 (2021) 1–11.
[4] S. Midha, S. Chawla, P.K. Garg, Modifiable and non-modifiable risk factors for pancreatic cancer: a review, Cancer Lett. 381 (2016) 269–277.
[5] A.P. Klein, Pancreatic cancer epidemiology: understanding the role of lifestyle and inherited risk factors, Nat. Rev. Gastroenterol. Hepatol. 18 (2021) 493–502.
[6] C.J. Halbrook, C.A. Lyssiotis, M. Pasca di Magliano, A. Maitra, Pancreatic cancer: advances and challenges, Cell 186 (2023) 1729–1754.
[7] Cancer Genome Atlas Research Network, Electronic address aadhe, cancer genome atlas research N. Integrated genomic characterization of pancreatic ductal adenocarcinoma, Cancer Cell 32 (2017) 185–203, e113.
[8] N. Waddell, et al., Whole genomes redefine the mutational landscape of pancreatic cancer, Nature 518 (2015) 495–501.
[9] N. Li, et al., lncRNA THAP9-AS1 promotes pancreatic ductal adenocarcinoma growth and leads to a poor clinical outcome via sponging miR-484 and interacting with YAP, Clin. Cancer Res. 26 (2020) 1736–1748.
[10] G. Rademaker, et al., Myoferlin controls mitochondrial structure and activity in pancreatic ductal adenocarcinoma, and affects tumor aggressiveness, Oncogene 37 (2018) 4398–4412.
[11] S. Gupta, et al., Lysosomal retargeting of Myoferlin mitigates membrane stress to enable pancreatic cancer growth, Nat. Cell Biol. 23 (2021) 232–242.
[12] J.L. Jimenez, R. Bashir, In silico functional and structural characterisation of ferlin proteins by mapping disease-causing mutations and evolutionary information onto three-dimensional models of their C2 domains, J. Neurol. Sci. 260 (2007) 114–123.
[13] C. Leung, C. Yu, M.I. Lin, C. Tognon, P. Bernatchez, Expression of myoferlin in human and murine carcinoma tumors: role in membrane repair, cell proliferation, and tumorigenesis, Am. J. Pathol. 182 (2013) 1900–1909.
[14] Y. He, et al., A potent and selective small molecule inhibitor of myoferlin attenuates colorectal cancer progression, Clin. Transl. Med. 11 (2021) e289.
[15] B. Kalyanaraman, et al., Measuring reactive oxygen and nitrogen species with fluorescent probes: challenges and limitations, Free Radic. Biol. Med. 52 (2012) 1–6.
[16] F. Yao, et al., A targetable LIFR-NF-κB-LCN2 axis controls liver tumorigenesis and vulnerability to ferroptosis, Nat. Commun. 12 (2021) 7333.
[17] J. Liu, et al., NUPR1 is a critical repressor of ferroptosis, Nat. Commun. 12 (2021) 647.
[18] X. Xiao, B.S. Yeoh, M. Vijay-Kumar, Lipocalin 2: an emerging player in iron homeostasis and inflammation, Annu. Rev. Nutr. 37 (2017) 103–130.
[19] J. Liu, et al., NUPR1 is a critical repressor of ferroptosis, Nat. Commun. 12 (2021).
[20] N. Chaudhary, et al., Lipocalin 2 expression promotes tumor progression and therapy resistance by inhibiting ferroptosis in colorectal cancer, Int. J. Cancer 149 (2021) 1495–1511.
[21] J. Jiang, J. Zhu, P. Qiu, J. Ni, W. Zhu, X. Wang, HNRNPA2B1-mediated m6A modification of FOXM1 promotes drug resistance and inhibits ferroptosis in endometrial cancer via regulation of LCN2, Funct. Integr. Genom. 24 (2023) 3.
[22] Y. Sun, et al., NGAL expression is elevated in both colorectal adenoma-carcinoma sequence and cancer progression and enhances tumorigenesis in xenograft mouse models, Clin. Cancer Res. 17 (2011) 4331–4340.
[23] W. Zhang, et al., Epigenetic induction of lipocalin 2 expression drives acquired resistance to 5-fluorouracil in colorectal cancer through integrin beta3/SRC pathway, Oncogene 40 (2021) 6369–6380.
[24] J. Yang, et al., Lipocalin 2 promotes breast cancer progression, Proc. Natl. Acad. Sci. U. S. A 106 (2009) 3913–3918.
[25] J. Morales-Valencia, L. Lau, T. Marti-Nin, U. Ozerdem, G. David, Therapy-induced senescence promotes breast cancer cells plasticity by inducing Lipocalin-2 expression, Oncogene 41 (2022) 4361–4370.
[26] Y. Chi, et al., Cancer cells deploy lipocalin-2 to collect limiting iron in leptomeningeal metastasis, Science 369 (2020) 276–282.
[27] O. Adler, et al., Reciprocal interactions between innate immune cells and astrocytes facilitate neuroinflammation and brain metastasis via lipocalin-2, Nat. Cancer 4 (2023) 401–418.
[28] U. Jayachandran, H. Grey, A.G. Cook, Nuclear factor 90 uses an ADAR2-like binding mode to recognize specific bases in dsRNA, Nucleic Acids Res. 44 (2016) 1924–1936.
[29] W. Jiang, et al., Regulation of cell cycle of hepatocellular carcinoma by NF90 through modulation of cyclin E1 mRNA stability, Oncogene 34 (2015) 4460–4470.
[30] S. Sur, H. Nakanishi, R. Steele, D. Zhang, M.A. Varvares, R.B. Ray, Long non-coding RNA ELDR enhances oral cancer growth by promoting ILF3-cyclin E1 signaling, EMBO Rep. 21 (2020) e51042.
[31] K. Li, et al., ILF3 is a substrate of SPOP for regulating serine biosynthesis in colorectal cancer, Cell Res. 30 (2020) 163–178.
[32] J. Liu, et al., The macrophage-associated LncRNA MALR facilitates ILF3 liquid-liquid phase separation to promote HIF1alpha signaling in esophageal cancer, Cancer Res. 83 (2023) 1476–1489.
[33] R. Wiener, X. Zhang, T. Wang, C. Wolberger, The mechanism of OTUB1-mediated inhibition of ubiquitination, Nature 483 (2012) 618–622.
[34] X. Han, C. Ren, C. Lu, P. Qiao, T. Yang, Z. Yu, Deubiquitination of MYC by OTUB1 contributes to HK2 mediated glycolysis and breast tumorigenesis, Cell Death Differ. 29 (2022) 1864–1873.
[35] T. Liu, L. Jiang, O. Tavana, W. Gu, The deubiquitylase OTUB1 mediates ferroptosis via stabilization of SLC7A11, Cancer Res. 79 (2019) 1913–1924.
[36] D. Li, et al., CST1 inhibits ferroptosis and promotes gastric cancer metastasis by regulating GPX4 protein stability via OTUB1, Oncogene 42 (2023) 83–98.
[37] Y. Xu, et al., Targeting the Otub1/c-Maf axis for the treatment of multiple myeloma, Blood 137 (2021) 1478–1490.
[38] T. Zhang, et al., A small molecule targeting myoferlin exerts promising anti-tumor effects on breast cancer, Nat. Commun. 9 (2018) 3726.
[39] H. Gu, et al., Discovery of 1,5-diaryl-1,2,4-triazole derivatives as myoferlin inhibitors and their antitumor effects in pancreatic cancer, Future Med. Chem. 14 (2022) 1425–1440.
[40] P. Bhandari, N. Kumar, B. Singh, P.S. Ahuja, Online HPLC-DPPH method for antioxidant activity of Picrorhiza kurroa Royle ex Benth. and characterization of kutkoside by ultra-performance LC-electrospray ionization quadrupole time-of-flight mass spectrometry, Indian J. Exp. Biol. 48 (2010) 323–328.
[41] R. Kumar, Y.K. Gupta, S. Singh, S. Arunraja, Picrorhiza kurroa inhibits experimental arthritis through inhibition of pro-inflammatory cytokines, angiogenesis and MMPs, Phytother Res. 30 (2016) 112–119.
[42] H. Yao, J. Yan, L. Yin, W. Chen, Picroside II alleviates DSS-induced ulcerative colitis by suppressing the production of NLRP3 inflammasomes through NF-kappaB signaling pathway, Immunopharmacol. Immunotoxicol. 44 (2022) 437–446.
[43] D. Soni, A. Grover, "Picrosides" from Picrorhiza kurroa as potential anti-carcinogenic agents, Biomed. Pharmacother. 109 (2019) 1680–1687.
[44] C. Lou, Z. Zhu, X. Xu, R. Zhu, Y. Sheng, H. Zhao, Picroside II, an iridoid glycoside from Picrorhiza kurroa, suppresses tumor migration, invasion, and angiogenesis in vitro and in vivo, Biomed. Pharmacother. 120 (2019) 109494.
[45] F.J. Meng, Z.W. Hou, Y. Li, Y. Yang, B. Yu, The protective effect of picroside II against hypoxia/reoxygenation injury in neonatal rat cardiomyocytes, Pharm. Biol. 50 (2012) 1226–1232.
[46] X. Piao, B. Liu, L. Guo, F. Meng, L. Gao, Picroside II shows protective functions for severe acute pancreatitis in rats by preventing NF-κB-Dependent autophagy, Oxid. Med. Cell. Longev. 2017 (2017) 7085709.
[47] J.D. Hayes, A.T. Dinkova-Kostova, K.D. Tew, Oxidative stress in cancer, Cancer Cell 38 (2020) 167–197.